



# Development of multi-group Monte-Carlo transport and depletion coupling calculation method and verification with metal-fueled fast reactor

Hui Guo<sup>1</sup> · Yi-Wei Wu<sup>1</sup> · Qu-Fei Song<sup>1</sup> · Yu-Yang Shen<sup>1</sup> · Han-Yang Gu<sup>1</sup>

Received: 10 February 2023 / Revised: 22 May 2023 / Accepted: 4 July 2023 / Published online: 14 November 2023

© The Author(s), under exclusive licence to China Science Publishing & Media Ltd. (Science Press), Shanghai Institute of Applied Physics, the Chinese Academy of Sciences, Chinese Nuclear Society 2023

## Abstract

The accurate modeling of depletion, intricately tied to the solution of the neutron transport equation, is crucial for the design, analysis, and licensing of nuclear reactors and their fuel cycles. This paper introduces a novel multi-group Monte-Carlo depletion calculation approach. Multi-group cross-sections (MGXS) are derived from both 3D whole-core model and 2D fuel subassembly model using the continuous-energy Monte-Carlo method. Core calculations employ the multi-group Monte-Carlo method, accommodating both homogeneous and specific local heterogeneous geometries. The proposed method has been validated against the MET-1000 metal-fueled fast reactors, using both the OECD/NEA benchmark and a new refueling benchmark introduced in this paper. Our findings suggest that microscopic MGXS, produced via the Monte-Carlo method, are viable for fast reactor depletion analyses. Furthermore, the locally heterogeneous model with angular-dependent MGXS offers robust predictions for core reactivity, control rod value, sodium void value, Doppler constants, power distribution, and concentration levels.

**Keywords** Monte-Carlo · Multi-group cross-section generation · Depletion · Fast reactors · Metallic fuel

## 1 Introduction

Depletion, also known as burnup or transmutation, is a time-dependent process in which nuclides transform due to nuclear reactions and spontaneous radioactive decay [1]. Modeling depletion is crucial for the design, analysis, and licensing of nuclear reactors and their fuel cycles, as it is intimately tied to the solution of the neutron transport equation. The Monte-Carlo (MC) method offers a versatile approach to tackle neutron transport challenges. It accommodates both continuous-energy (CE) and multi-group cross-sections (MGXS) and allows for modeling using either constructive solid geometry (CSG) or computer-aided design

(CAD) representations. This flexibility ensures accurate and high-fidelity modeling of nuclear reactors and related systems.

The depletion capabilities have been implemented in many Monte-Carlo codes by coupling with their CE transport calculation including MCNP6 [2], MC21 [3], Serpent [4], JMCT [5], RMC [6], and OpenMC [1], etc. The CE depletion calculation scheme determines reaction rates for all nuclides within depletable zones. These rates subsequently assist in solving the Bateman equations. Despite the detailed physics modeling, which grants the CE scheme enhanced simulation precision, it demands repeated CE transport calculations. This repetition leads to high computational costs, especially given the numerous reaction rate tallies required for the discretization of depletable zones and nuclides [7]. Any modifications to core parameters necessitate a complete recalculation of depletion demanding substantial computational resources, especially during the general design phase of a nuclear reactor.

Conversely, the multi-group Monte-Carlo (MGMC) transport calculation, homogenizes the space and utilizes MGXS. This method is adopted by platforms such as

---

This work was supported by the National Natural Science Foundation of China (Nos. 12105170, 12135008), Science and Technology on Reactor System Design Technology Laboratory.

✉ Han-Yang Gu  
guhanyang@sjtu.edu.cn

<sup>1</sup> School of Nuclear Science and Engineering, Shanghai Jiao Tong University, Shanghai 200240, China

MVP/GMVP II [8], Shift [9], MC3 [10], RMC [6], and OpenMC [11]. It offers the advantage of reduced computational costs while retaining flexibility in geometric modeling. One key focus in multiphysics analysis is the local heterogeneity at the core calculation level [12]. This research examines the locally heterogeneous modeling of absorbers in contrast to the conventional homogeneous modeling of all assemblies in multi-group core solutions.

The effectiveness of MG calculations largely hinges on the generation of MGXS. While MGXS is foundational for many deterministic neutron transport codes and MGMC calculations, its generation via CEMC tallies has gained traction. Platforms such as SERPENT [13], MCNP6 [2], McCARD [14], RMC [6], and OpenMC [15] have incorporated this method. It integrates resonance self-shielding and multi-level lattice calculations, providing an alternative to deterministic approaches. Given the intricate geometries and mixed spectra in contemporary nuclear system designs, there is increasing interest in this method. Although past research [16–19] has often employed 2D assemblies/clusters or 3D assemblies to generate macroscopic cross-sections, this study delves into 3D whole-core modeling for generating microscopic MGXS. This approach becomes even more pertinent for smaller reactors, emphasizing the significance of neutron leakage and spatial effects.

In our previous work, we verified the generation of MGXS using OpenMC [20] and its integration with a MGMC transport solver and a diffusion solver. This verification was performed on a sodium fast reactor (SFR) for static analyses without burnup [17]. The present work's objective is to develop and verify a transport depletion coupling calculation method. This method utilizes MGXS generated in

3D whole-core models using the CE MC technique and core calculations executed with the MGMC method that incorporates locally heterogeneous models. Additionally, this research will explore the impact of angle-dependent and burnup-dependent MGXS.

The remaining paper is organized as follows: Section 2 elaborates on the calculation scheme adopted in this study, encompassing the strategies for cross-section generation, core calculation, and depletion resolution. Section 3 presents the numerical benchmarks for the proposed scheme. Section 4 concludes the paper, summarizing key findings, discussing potential limitations, and hinting at future research directions.

## 2 Multi-group Monte-Carlo depletion scheme

Figure 1 provides a comprehensive overview of the MG depletion scheme proposed herein. This scheme encapsulates effective cross-section generation, core calculation, and depletion resolution. These critical phases will be elucidated in the subsequent sections. It is noteworthy that the MG model's design, which includes its geometry, materials, and cross-sections, is facilitated by OpenMC's Python API. This not only streamlines model construction but also offers flexibility in toggling between the CE and MG schemes.

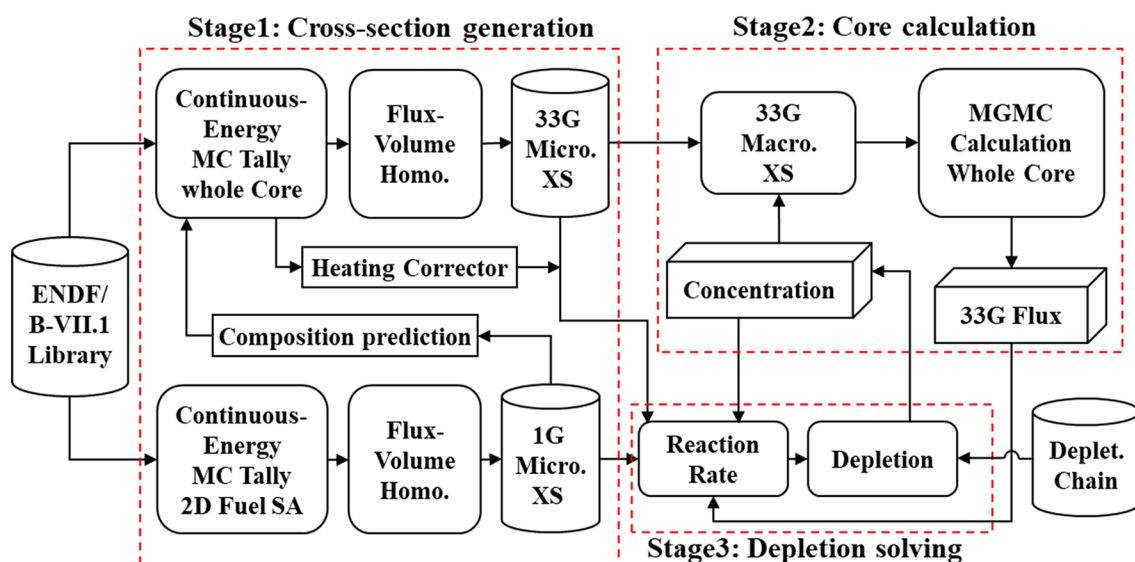
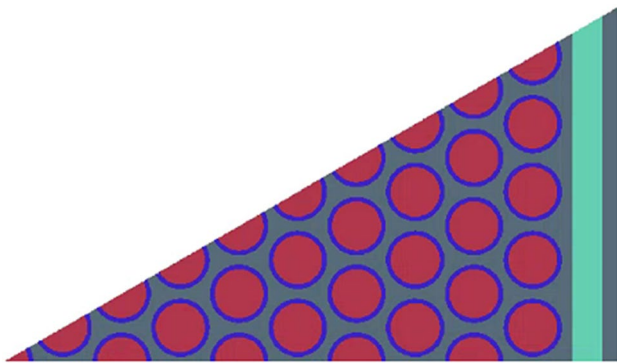


Fig. 1 Schematic of multi-group Monte-Carlo burnup calculation scheme

## 2.1 Cross-section generation stage

### 2.1.1 Single-group microscopic cross-sections for depletion

The 1-group cross-sections, essential for depletion calculations, are derived from OpenMC's modeling of the 2D fuel subassembly (SA) as depicted in Fig. 2. This is achieved using flux-volume homogenization techniques. During this phase, 1-group  $(n, f)$ ,  $(n, \gamma)$ ,  $(n, \alpha)$ ,  $(n, p)$ ,  $(n, 2n)$ ,  $(n, 2n)$ ,  $(n, 3n)$ , and  $(n, 4n)$  microscopic cross-sections for all nuclides listed in the ENDF/B-VII.1 library are generated. These cross-sections align with those utilized in the CE depletion scheme. The rationale behind employing this 2D geometry is to ensure representative flux characteristics, pivotal for generating cross-sections for depletion. Such supercell geometries are prevalently employed in deterministic processes



**Fig. 2** (Color online) Layout of 2D fuel subassembly of MET-1000 for 1-group cross-section generation

for generating multi-group cross-sections for transport calculations [21].

### 2.1.2 Multi-group microscopic cross-sections for whole-core transport and depletion

These cross-sections are produced from OpenMC's modeling of a 3D heterogeneous core, as visualized in Fig. 3a. This comprehensive core model is adept at conducting intricate depletion calculations and generating MGXS for every burnup step. The impact of burnup on the microscopic MGXS of metal-fueled SFRs is delved into in Sect. 3.1.2. While generating burnup-dependent MGXS would elevate the computational demands, this study leverages burnup-independent MGXS unless stated otherwise. In a fresh core, there is an absence of fission products and certain heavy nuclides. For depletable materials, material composition is anticipated using the 1-group cross-sections from the preceding phase. The flux level is discerned from the 2D fuel subassembly, reflecting the core's average power density. The irradiation duration equates to half of the core's total residence time. Depletion calculations, employing the predictor method, are executed using OpenMC's inbuilt solver. Both the chain and time step mirror the core's comprehensive calculations. Consequently, the composition closely mirrors an average burnup state, leading to the generation of MGXS in a core state with an average fuel burnup.

Microscopic cross-sections are generated using flux-volume homogenization techniques by simulating the heterogeneous core with predicted compositions through CE calculations. This procedure simultaneously produces the microscopic cross-sections of heavy nuclides, structural nuclides, and key fission products from all core materials. For the core transport calculation in Stage 2, 33-group total

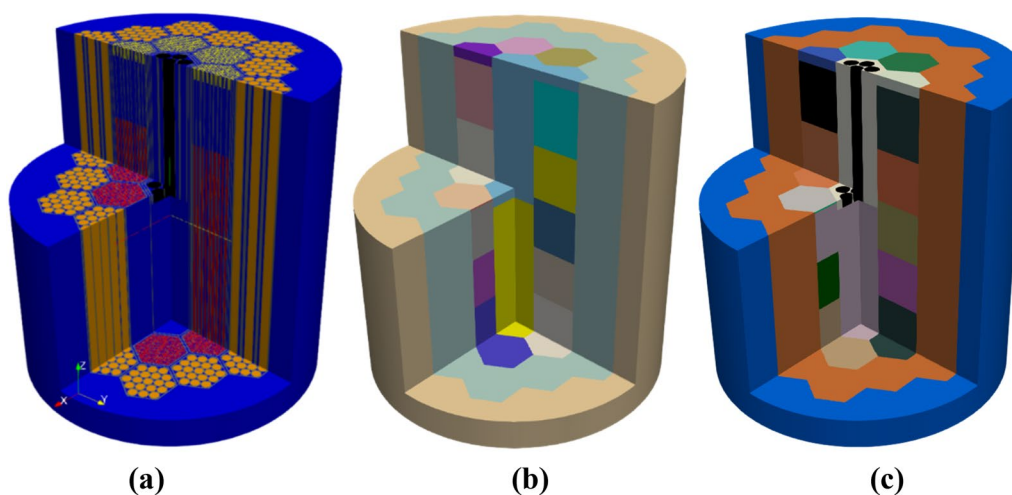


**Fig. 3** (Color online) Symbolic illustrations of 3D core model for cross-section generation and multi-group core calculation. (a) Heterogeneous model; (b) Homogenous model; (c) Locally heterogeneous model

( $\sigma_t$ ), absorption ( $\sigma_a$ ), fission production ( $\nu\sigma_f$ ), scattering multiplicity ( $\sigma_s$ ), and fission emission spectrum ( $\chi$ ) microscopic cross-sections are employed. The scattering multiplicity equips OpenMC’s multi-group mode with the requisite data for accurate treatment of scattering multiplication (specifically, (n, xn) reactions). This data also elucidates how this multiplication varies based on both incoming and outgoing neutron energies.

In OpenMC [15], the angle-independent macroscopic cross-section  $\Sigma_{x,i,k,g}$  for a nuclide  $i$  in spatial region  $k$  and energy domain  $[E_{g-1}, E_g]$ , is determined by the ratio of group-wise reaction rates  $\langle \Sigma_{x,i}, \psi \rangle_{k,g}$  to fluxes  $\langle \psi \rangle_{k,g}$  as measured by the track-length estimators.

$$\Sigma_{x,i,k,g} = \frac{\Sigma_{x,i}\psi_{k,g}}{\psi_{k,g}} \tag{1}$$

$$\langle \Sigma_{x,i}, \psi \rangle_{k,g} = \int_{r \in V_k} \mathbf{dr} \int_{4\pi} \mathbf{d}\Omega \int_{E_g}^{E_{g-1}} dE \Sigma_x(r, E) \psi(r, E, \Omega) \tag{2}$$

$$\langle \psi \rangle_{k,g} = \int_{r \in V_k} \mathbf{dr} \int_{4\pi} \mathbf{d}\Omega \int_{E_g}^{E_{g-1}} dE \psi(r, E, \Omega) \tag{3}$$

Scattering data is represented through a Legendre expansion. For consistency, the scattering matrix is derived as the product of the scattering cross-sections  $\Sigma_{s,i,k,g}$ , which are determined by the track-length estimator, and the group-to-group probabilities  $P_{s\uparrow,i,k,g' \rightarrow g}$ :

$$\Sigma_{s\ell,i,k,g' \rightarrow g} = \Sigma_{s,i,k,g'} \times P_{s\ell,i,k,g' \rightarrow g}, \tag{4}$$

where the scattering probability matrix is computed from analog tallies:

$$P_{s\ell,i,k,g' \rightarrow g} = \frac{\Sigma_{s\ell,i}, \psi_{k,g' \rightarrow g}}{\Sigma_{s0,i}, \psi_{k,g' \rightarrow g}}, \tag{5}$$

$$\Sigma_{s\ell,i}, \phi_{k,g' \rightarrow g} = \int_{r \in V_k} \mathbf{dr} \int_{4\pi} \mathbf{d}\Omega' \int_{E_{g'}}^{E_{g'-1}} dE' \int_{4\pi} \mathbf{d}\Omega \int_{E_g}^{E_{g-1}} dEP_\ell(\Omega \cdot \Omega') \Sigma_s(r, E' \rightarrow E, \Omega' \cdot \Omega) \psi(r, E', \Omega'). \tag{6}$$

This consistent formulation of higher-order scattering ensures that exact preservation of the reaction rate balance, as other cross-sections are determined using a track-length estimator. Additionally, the formulation takes into account the scattering multiplicity effect, capturing the effect of neutron multiplication stemming from (n, xn) reactions.

The fission spectrum is obtained by using:

$$\chi_g = \frac{\langle \nu\sigma_{f,g'} \psi \rangle}{\langle \nu\sigma_f \psi \rangle}, \tag{7}$$

$$\langle \nu\Sigma_{f,g' \rightarrow g} \phi \rangle = \int_{r \in V} \mathbf{dr} \int_{4\pi} \mathbf{d}\Omega' \int_0^\infty dE' \int_{E_g}^{E_{g-1}} dE \chi(E) \nu\Sigma_f(r, E') \psi(r, E', \Omega'), \tag{8}$$

$$\langle \nu\Sigma_f \phi \rangle = \int_{r \in V} \mathbf{dr} \int_{4\pi} \mathbf{d}\Omega' \int_0^\infty dE' \int_0^\infty dE \chi(E) \nu\Sigma_f(r, E') \psi(r, E', \Omega'). \tag{9}$$

Traditionally, both the rate and flux are tallied across the entire angular space, leading to MGXS that are independent of the incident neutron angles. This approach is commonly referred to as the flux separability approximation (FSA) [22]. However, when there is correlation between angle- and energy-dependence of the neutron flux, the FSA can potentially introduce significant errors [22]. OpenMC offers a more rigorous approach by generating angle-dependent MGXS data, essentially providing MGXS data that explicitly relaxes the constraints of the FSA. For a given angle bin  $\omega$ , the MGXS are defined as:

$$\Sigma_{x,i,k,g,\omega} = \frac{\Sigma_{x,i}, \psi_{k,g,\omega}}{\psi_{k,g,\omega}}, \tag{10}$$

$$\langle \Sigma_{x,i}, \psi \rangle_{k,g,\omega} = \int_{r \in V_k} \mathbf{dr} \int_{\omega} \mathbf{d}\Omega \int_{E_g}^{E_{g-1}} dE \Sigma_x(r, E) \psi(r, E, \Omega), \tag{11}$$

$$\langle \psi \rangle_{k,g,\omega} = \int_{r \in V_k} \mathbf{dr} \int_{\omega} \mathbf{d}\Omega \int_{E_g}^{E_{g-1}} dE \psi(r, E, \Omega). \tag{12}$$

Utilizing angle-dependent MGXS data to relax the constraints of the FSA has been shown to enhance accuracy, especially in 1-D and 2D symbolic problems [22]. In this paper, we will probe the effects of FSA on MC transport within a 3D realistic fast reactor core. Herein, the term 1-angle scheme denotes that MGXS is generated under the FSA. In contrast, the 32-angle scheme signifies MGXS generation that relaxes FSA, achieved by evenly dividing the angle into 8 azimuthal and 4 polar angles.

Given this setup, the nuclide-specific microscopic cross-section is formulated as:

$$\sigma_{x,i,k,g} = \frac{\Sigma_{x,i,k,g}}{N_{i,k}}. \tag{13}$$

Under this definition, parameters such as  $\sigma_t$ ,  $\sigma_a$ ,  $\nu\sigma_f$ ,  $\sigma_s$ , and  $\chi$  of all nuclides are computed. Additionally, we account for the radioactive capture  $\sigma_c$  and  $\kappa\sigma_f$  of all heavy nuclides throughout the core. For the remaining reactions and nuclides, 1-group microscopic cross-sections are utilized during the depletion calculation in Stage 3.

Gamma heating constitutes a significant portion of the core’s power. Gamma-heating values are derived from gamma KERMA values and gamma production cross-sections, as

generated by the multi-group cross-section generation code [23, 24]. In the multi-group transport calculation detailed in Sect. 2.2, only kappa-fission ( $H_{\text{kappa}}$ ) for flux normalization. The normalization factor ( $f_{\text{MG}}$ ) is determined as:

$$f_{\text{MG}} = \frac{P}{H_{\text{kappa}}}. \quad (14)$$

While  $H_{\text{kappa}}$  represents the recoverable energy from fissions, energy contributions from neutron heating and secondary photons are also vital. Within OpenMC's CE depletion scheme, normalization relies on localized heating ( $H_{\text{local}}$ ), which accounts for indirect energy, such as neutron heating and energy from secondary photons, are taken into account. In CE calculation, the normalization factor ( $f_{\text{CE}}$ ) is obtained by dividing the core power ( $P$ ) by the observed heating rate ( $H_{\text{local}}$ ):

$$f_{\text{CE}} = \frac{P}{H_{\text{local}}}. \quad (15)$$

The  $H_{\text{kappa}}$  is typically less than  $H_{\text{local}}$ , its normalization can introduce errors. Consequently, we tally both  $H_{\text{local}}$  and  $H_{\text{kappa}}$  for the entire core. Their ratio serves as a heating correction factor ( $HC$ ) during the core calculation stage.

$$HC = \frac{H_{\text{kappa}}}{H_{\text{local}}} \quad (16)$$

The amended normalization factor in the MG stage becomes:

$$f_{\text{MG}}^{\text{corrector}} = f_{\text{MG}} \cdot HC. \quad (17)$$

Other tallies, for instance, the flux, undergo multiplication by the normalization factor to render values in conventional units. Therefore, a flux acquired without HC is greater than one with HC. Our heating corrector method is a "global" correction approach, contrasting with gamma-heating calculations rooted in gamma data generation and distribution. The implications of heating correction are discussed further in Sects. 3.1.2 and 3.1.6.

## 2.2 Core calculation stage

The MGMC core transport calculations rely on macroscopic cross-sections, which are formulated using multi-group microscopic cross-sections and concentrations determined during the depletion resolution phase.

The geometry for the MGMC core calculation is constructed using the CSG method. The core calculation employs both homogeneous (Homo, as depicted in Fig. 3b) and locally heterogeneous (LHete, as shown in Fig. 3c) modeling. In the homogeneous approach, each subassembly sector is unified into a single macroscopic zone. Despite its distinct methodology, the MG scheme retains a

similar degree of geometric description freedom as the CE scheme. With the locally heterogeneous modeling, specifics such as particular fuel rods, unique experimental structures, absorbers, burnable poisons, and more are precisely defined, while other regions undergo homogenization. In this study, absorber pellets within control rods are maintained in the locally heterogeneous model. While previous research explored this modeling with deterministic codes, it necessitated finer local meshes and considerably more computational resources [21]. However, the multi-group MC solver proficiently models local heterogeneity using the CSG method with only marginally increased computational demand.

Parameters such as the effective multiplication factor ( $k_{\text{eff}}$ ), power distribution, and 33-group flux distribution are derived from the MG core calculations. It is assumed that the power's relative distribution mirrors the kappa-fission distribution. The flux undergoes normalization using the total kappa-fission of the entire core and the heating correction factor from the preceding phase.

## 2.3 Depletion solving stage

The fission and capture reaction rates for heavy nuclides are ascertained by combining the 33-group microscopic cross-sections from the MGXS generation phase with the 33-group flux from the core transport calculation phase. For other nuclides, the reaction rates are determined by merging the 1-group microscopic cross-sections with the sum of the 33-group flux. These reaction rates, in conjunction with the depletion chain, facilitate the construction of the burnup matrix necessary for solving the Bateman equation. Following this, nuclide concentrations for each depletable material are updated.

OpenMC's built-in depletion solver evaluates matrix exponentials using the Chebyshev rational approximation method [1], a technique proposed in papers by Pusa [25, 26] and later integrated into OpenMC by Romano [1]. OpenMC encompasses multiple integration methods and depletion chains. This research employs the predictor method, which assumes a consistent burnup matrix over a burnup time step, across both the CE and MG schemes. The depletion chain encompasses transmutation patterns, decay data, and fission product (FP) yields, serving as crucial data for precise depletion calculations. This study utilizes two depletion chains available in OpenMC:

- The *full* chain, comprising 3820 nuclides, is sourced from the ENDF-format library.
- The *CASL* chain, encompassing 228 nuclides, is derived using the VERA depletion benchmark specification and adjusted decay branching ratios for select nuclides to maintain accurate nuclide production rates.

The primary distinction between these chains lies in their FP treatment. Most FPs with shorter half-lives are excluded in the *CASL* chain and are assimilated into their descendant nuclides. As per [27], the computation time for the CE scheme with the *full* chain is approximately double that of the *CASL* chain, with minimal reactivity variance. The *full* chain becomes particularly relevant when precise FP computations are requisite.

### 3 Results and discussions

This study emphasizes the numerical verification of the MET-1000 core, a 1000 MWth mid-sized metal-fueled SFR core, as derived from the benchmark by the OECD/NEA Working Party on Scientific Issues of Reactor Systems (WPRS) [28]. This benchmark was selected due to its diverse contributions from numerous international organizations, each employing different neutronic data libraries and transport codes. This diversity ensures a comprehensive feedback derived from a broad spectrum of neutronic simulations.

Section 3.1 presents the results from the OECD/NEA benchmark. Since the OECD/NEA benchmark encompasses only one cycle, an additional verification that examines multiple cycles with a batch-wise fuel refueling scenario is detailed in Sect. 3.2.

### 3.1 MET-1000 OECD/NEA benchmark

#### 3.1.1 Description of benchmark

The detailed specifications for the MET-1000 can be found in Ref. [28]. This model is rooted in the advanced burner reactor (ABR) core concept, which utilizes a ternary U–Pu–Zr metallic fuel. The layout of the MET-1000 core is presented in Fig. 4, which encompasses 72 inner driver fuel, 102 outer driver fuel SAs, 114 radial reflector SAs, 66 radial shielding SAs, and 19 control SAs. This core is grounded in current fast reactor technological know-how. Anticipated outcomes include core multiplication factors, sodium void worth, Doppler constant, effective delayed neutron fraction, average nuclide mass, and power distribution at both the beginning of cycle (BOC) and end of cycle (EOC). Excluding the effective delayed neutron fraction, subsequent discussions will explore other results from both the CE and MG schemes. The CE scheme results serve as a reference for the MG scheme, as they stem from the same modeling and nuclear data libraries, which encompass the ENDF/B-VII.1 cross-sections and *full* depletion chain.

The reference CE model of MET-1000 using OpenMC is shown in Fig. 4. This representation ensures all benchmark-specified structures are modeled without any oversimplifications. This exact model is also employed for the generation of MGXS across all zones simultaneously. The MG core simulation is undertaken with both Homo and LHete modeling, as illustrated in Fig. 5. The sole distinguishing factor between the Homo and LHete models is the LHete's explicit depiction of control rods within the 19 control SAs. For both

**Fig. 4** (Color online) Radial (a) and axial (b) layout of MET-1000 core. Remark: Control rods are symbolically presented in the radial layout, and positioned at the top of the fissile zone (as depicted in the axial layout) in the depletion simulation

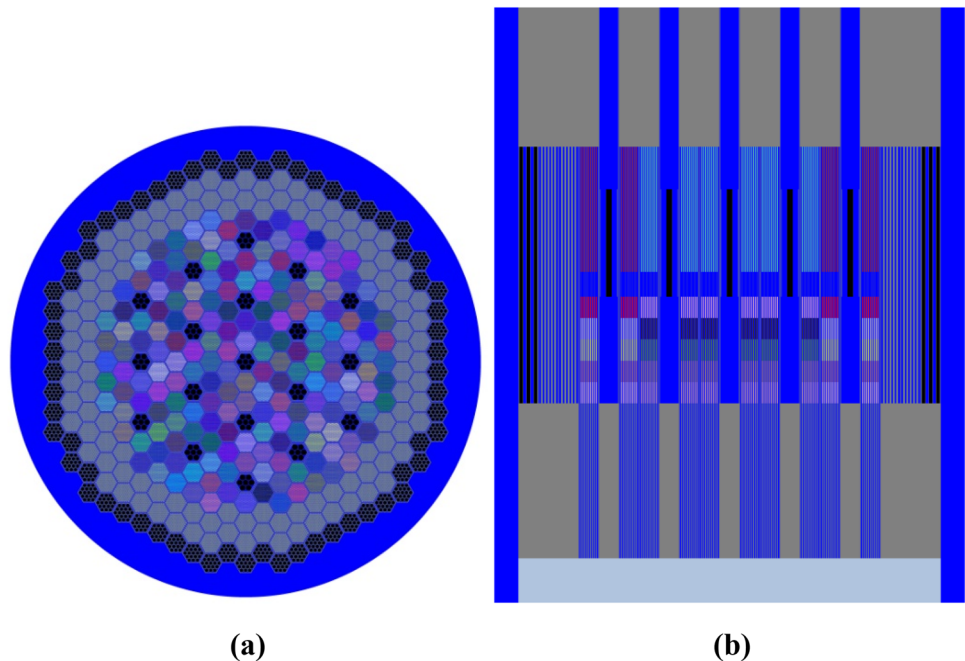
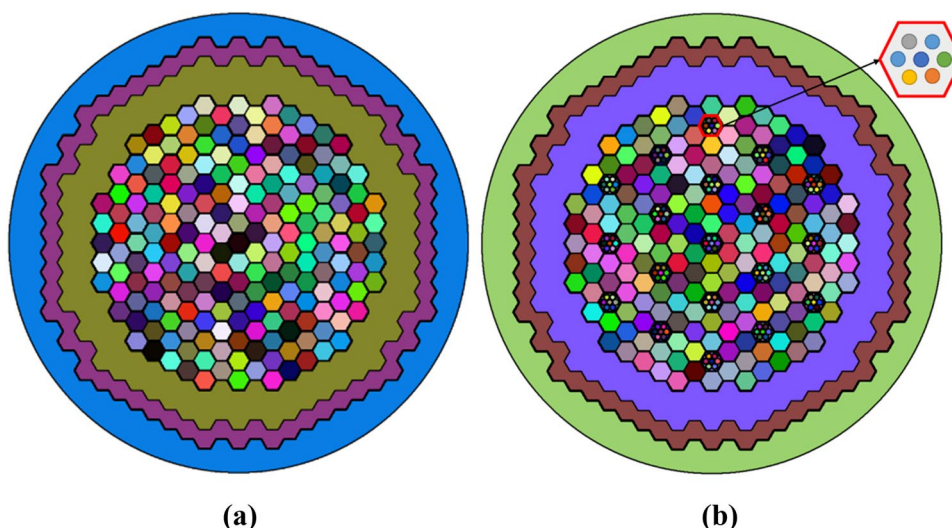


**Fig. 5** (Color online) Layout of homogenous (a) and locally heterogeneous (b) model for multi-group Monte-Carlo core calculation



CE and MG schemes, the cycle duration, set at 328.5 days, is evenly split into five steps. The fuel region undergoes a radial division into SA-by-SA and an axial division into 10 zones for each SA.

### 3.1.2 Reactivity

For the MET-1000 OECD/NEA benchmark, data from eight institutions yielded 20 distinct results. The core multiplication factor ( $k_{eff}$ ) and the burnup reactivity swing ( $\Delta\rho_{BU}$ ) derived from the OpenMC CE and MG modes are juxtaposed with the OECD/NEA outcomes in Table 1. The  $\Delta\rho_{BU}$  is defined as:

$$\Delta\rho_{BU} = 10^5 \left( \frac{1}{k_{eff}(BOC)} - \frac{1}{k_{eff}(EOC)} \right). \tag{18}$$

The OECD/NEA benchmark results exhibit an approximate deviation of 750 pcm in the multiplication factor and 422 pcm in the burnup reactivity swing. These discrepancies can be attributed to variations in simulation methodologies, model descriptions, and nuclear data libraries. All MG mode results from OpenMC align with the OECD/NEA findings

within a single standard deviation. However, the  $k_{eff}$  of the CE scheme at EOC extends beyond the deviation range specified in the OECD/NEA report. This divergence might arise from updates in nuclear data libraries and nuances in modeling details. In this study, by contrasting the MG scheme with the CE scheme, we mitigate the effects of modeling precision and nuclear data library variations. This approach provides a more fitting validation for the MG scheme proposed herein.

As illustrated in Fig. 6, employing the MG scheme with FSA results in an overestimation of core reactivity by approximately 1125 pcm at the BOC. By utilizing the 32-angle MGXS data, this overestimation reduces to 425 pcm. Notably, the angle-dependent MGXS data enhances the multiplication accuracy by approximately 700 pcm for the MET-1000 core.

By the EOC, there is a further rise in the overestimation of core reactivity with burnup: approximately 150 pcm for the 1-angle approach and 80 pcm for the 32-angle approach. This discrepancy in the  $k_{eff}$  prediction also influences the reactivity swing, leading the MG scheme to underestimate the burnup reactivity loss, as highlighted in

**Table 1** Core reactivity in MET-1000 OECD/NEA benchmark

	Effective multiplication factor		Burnup reactivity swing	
	$k_{eff}$ at BOC	$k_{eff}$ at EOC	$\Delta\rho_{BU}$ (pcm)	MG-CE (pcm)
OECD/NEA Report	$1.0355 \pm 0.0078$	$1.0123 \pm 0.0071$	$-2210 \pm 422$	–
CE	1.02907	1.00334	–2492	–
1-angle&Homo	1.04087	1.01610	–2342	150
32-angle&Homo	1.03326	1.00812	–2414	78
1-angle&LHete	1.04125	1.01649	–2340	152
32-angle&LHete	1.03366	1.00858	–2405	87

Remark: The statistical uncertainty of the OpenMC results in  $k_{eff}$  is approximately  $\pm 5$  pcm. The results of the OECD/NEA Report are from Ref. [28]

**Fig. 6** Trend of multiplication factor in MET-1000 OECD/NEA benchmark

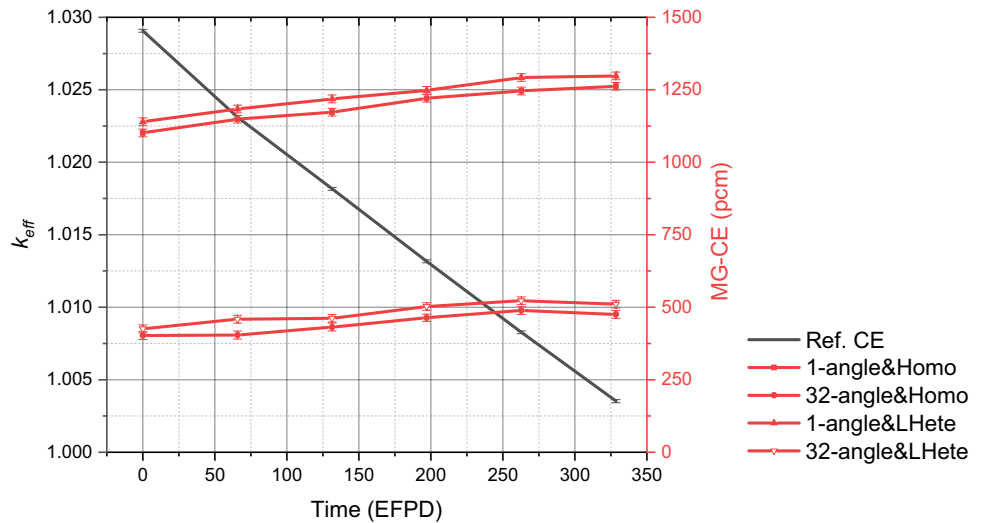


Table 1. The underlying causes of this deviation in burnup reactivity prediction will be explored subsequently.

It is noteworthy that the  $k_{eff}$  from the Homo scheme is approximately 40 pcm lower than that from the LHete scheme. This difference arises due to the Homo scheme's overestimation of the control rod's absorption capacity (refer to Sect. 3.1.3). However, the difference between the Homo and LHete schemes concerning burnup reactivity is minimal.

Table 2 provides a summary of the sensitivity of burnup reactivity swing across various scheme configurations. The designation 1-angle & Homo & woHC represents results obtained without incorporating heating correction. In the context of the MET-1000 core, the normalization factor, when determined by the total kappa-fission, is 1.04 times that of the factor derived from the total heating-local. As a result, the option without heating correction (*w/o* HC) overestimates burnup by approximately 4%. This translates to a rough effect of approximately  $| -2492 \times 4\% | \approx 100$  pcm in the burnup reactivity swing. Although the *w/o* HC option minimizes the discrepancy in burnup reactivity swing, it is a blend of multiple biases. The impact of the *w/o* HC

option on concentration prediction will be further explored in Sect. 3.1.6.

Two primary sources contribute to the variation in the prediction of burnup reactivity swing:

- (1) At the BOC, disparities in flux distribution and the spectrum between the MG and CE schemes can result in differences in reaction rates. This, in turn, affects the prediction of concentration distribution at the EOC. To validate this influence, the MG scheme is assessed with the EOC concentration deduced from the CE scheme. As evident from the 1-angle&LHete&CEConc and 32-angle&LHete&CEConc entries in Table 1, the EOC concentration from the CE scheme reduces the discrepancy in burnup reactivity swing by 88 and 53 pcm, respectively.
- (2) The assumption in this paper is that cross-sections remain constant with burnup. This approximation can introduce variations in the predicted core reactivity. To verify this, MG core calculations at both BOC and EOC are performed using corresponding BOC and EOC MGXS data. For the 32-angle & LHete case, the

**Table 2** Sensitivity of core reactivity to scheme options in MET-1000 OECD/NEA benchmark

	Effective multiplication factor		Burnup reactivity swing	
	$k_{eff}$ at BOC	$k_{eff}$ at EOC	$\Delta\rho_{BU}$ (pcm)	MG-CE (pcm)
1-angle&Homo & <i>w/o</i> HC	1.04087	1.01510	-2438	54
1-angle&LHete & CEConc	1.04125	1.01558	-2428	64
32-angle&LHete & CEConc	1.03366	1.00804	-2458	34
1-angle&LHete & CEConc&VarXS	1.04149	1.01557	-2451	42
32-angle&LHete & CEConc&VarXS	1.03390	1.00794	-2491	1

Remark: *w/o* HC is the results without heating correction. CEconc is the MG core calculation with EOC concentration predicted from the CE scheme. VarXS is the MG core calculation at BOC with MGXS generated with the core state at BOC, at EOC with MGXS generated with addition nuclides predicted at EOC

BOC MGXS data introduces a reactivity increment of approximately 24 pcm from 1.03366 to 1.03390, amplifying the BOC bias. Employing “variable” MGXS data ameliorates the burnup reactivity prediction by approximately 30 pcm. Although the subsequent discussions utilize burnup-independent MGXS, the influence of burnup on MGXS warrants further examination in different reactor contexts.

When these two factors are accurately addressed, the 32-angle&LHete&CEConc&VarXS displays a negligible deviation from the reference value.

### 3.1.3 Control rod worth

The worth of the control rod, denoted as  $\Delta\rho_{CR}$ , is calculated based on the difference in core reactivity when all control rods are fully withdrawn (position  $z_{out}$ , at the top of the fissile zone) versus when they are fully inserted (position  $z_{in}$ , at the bottom of the fissile zone):

$$\Delta\rho_{CR} = 10^5 \left( \frac{1}{k_{eff}(z_{out})} - \frac{1}{k_{eff}(z_{in})} \right). \tag{19}$$

Table 3 displays the worth of the control rod at both the BOC and EOC. According to the MET-1000 OECD/NEA benchmark, control rods are treated as non-depletable. The observed increase in control rod worth primarily stems from changes in the power/flux distribution as illustrated in Fig. 7. All results from OpenMC, whether derived from the CE or MG modes, align within one standard deviation of the OECD/NEA results.

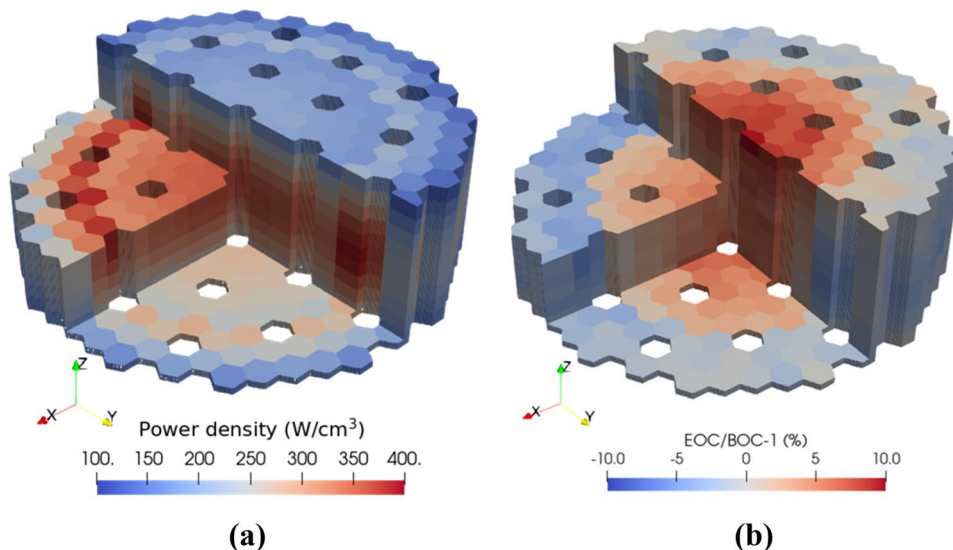
Comparing schemes, the homogeneous (Homo) model overestimates the control rod worth by approximately 5.3% relative to the CE scheme. Transitioning to the locally heterogeneous (LHete) model reduces this overestimation to 1.4%. These findings bear resemblance to those from MG calculations in the CEFR, a 65 MWth UOX experimental reactor [17] For the increase in control worth, the Homo and LHete schemes overestimate by approximately 85 pcm and 48 pcm, respectively. Relaxing the FSA slightly refines the results for the LHete scheme but seems to have minimal impact on the Homo scheme.

**Table 3** Control rod worth in MET-1000 OECD/NEA benchmark (unit: pcm)

	BOC		EOC		EOC-BOC	
	$\Delta\rho_{CR}$	MG-CE	$\Delta\rho_{CR}$	MG-CE	$\Delta\rho_{CR}$	MG-CE
OECD/NEA Report	$19,697 \pm 2087$	–	$20,497 \pm 2228$	–	–	–
CE	18,257	–	18,932	–	675	–
1-angle & Homo	19,220	963	19,978	1047	758	83
32-angle & Homo	19,223	966	19,985	1053	762	87
1-angle & LHete	18,516	259	19,238	307	722	48
32-angle & LHete	18,432	175	19,155	223	723	48

Remark: The statistical uncertainty of the OpenMC results is approximately  $\pm 5$  pcm. The results of the OECD/NEA Report are from Ref. [28]

**Fig. 7** (Color online) 3D power distribution at BOC (a) and power variation at EOC (b) from continuous-energy Monte-Carlo simulations in MET-1000 OECD/NEA benchmark



### 3.1.4 Sodium void worth and Doppler constant

The sodium void worth is a crucial safety parameter for studying the core physics of fast reactors. Within this benchmark, the sodium void worth is characterized by the difference in reactivity between sodium voided and normal states as follows:

$$\Delta\rho = \rho_{\text{void}} - \rho_{\text{normal}}, \tag{20}$$

where the subscripts void and normal denote the sodium voided and normal states, respectively. The benchmark defines the sodium voided state by voiding all sodium within the fissile zones. For the MET-1000, the sodium void worth is positive and tends to increase with burnup.

In our approach, the sodium void worth is calculated using the same MGXS microscopic library as the normal state. However, during the macroscopic library homogenization process, <sup>23</sup>Na is set to zero. All results from OpenMC, in both the CE and MG modes, align within one standard deviation of the OECD/NEA results. The 1-angle scheme exhibits an overestimation of the sodium void worth by approximately 110 pcm, whereas the 32-angle scheme underestimates by approximately 22 pcm. There is a noticeable 132 pcm difference arising from the FSA. The disparity between the LHete and Homo schemes remains minimal (Table 4).

The Doppler constant, vital for understanding reactor behavior under varying temperatures, is defined as follows:

$$\Delta\rho = \frac{\rho_{\text{high}} - \rho_{\text{normal}}}{\ln\left(\frac{T_{\text{high}}}{T_{\text{normal}}}\right)}, \tag{21}$$

where the subscript high refers to the perturbed core state. As per the OECD/NEA benchmark, the heightened fuel temperature is double the standard, equating to 1614 K. It is essential to note that this temperature might exceed the fuel's melting point [29], thus its use is strictly for numerical benchmarking purposes.

In our methodology, MGXS data for all structural components in perturbed states are regenerated based on the respective elevated temperatures. The Doppler constant comparisons are available in Table 5. Both the CE and MG scheme results comply with the OECD/NEA outcomes within a standard deviation. At the BOC, the MG results are in line with the CE outputs, also within one standard deviation. While the Doppler constant diminishes with burnup according to the CE scheme, only the 32-angle MG scheme accurately predicts this trend. In contrast, the 1-angle scheme tends to underestimate the Doppler constant's variation.

**Table 4** Sodium void worth in MET-1000 OECD/NEA benchmark (unit: pcm)

	BOC		EOC		EOC-BOC	
	$\Delta\rho_{\text{void}}$	MG-CE	$\Delta\rho_{\text{void}}$	MG-CE	$\Delta\rho_{\text{void}}$	MG-CE
OECD/NEA Report	2024 ± 407	–	2146 ± 435	–	/	–
CE	1991	–	2140	–	148	–
1-angle & Homo	2107	116	2254	115	147	–1
32-angle & Homo	1967	–24	2117	–23	150	2
1-angle & LHete	2099	108	2254	114	155	7
32-angle & LHete	1970	–22	2130	–10	160	12

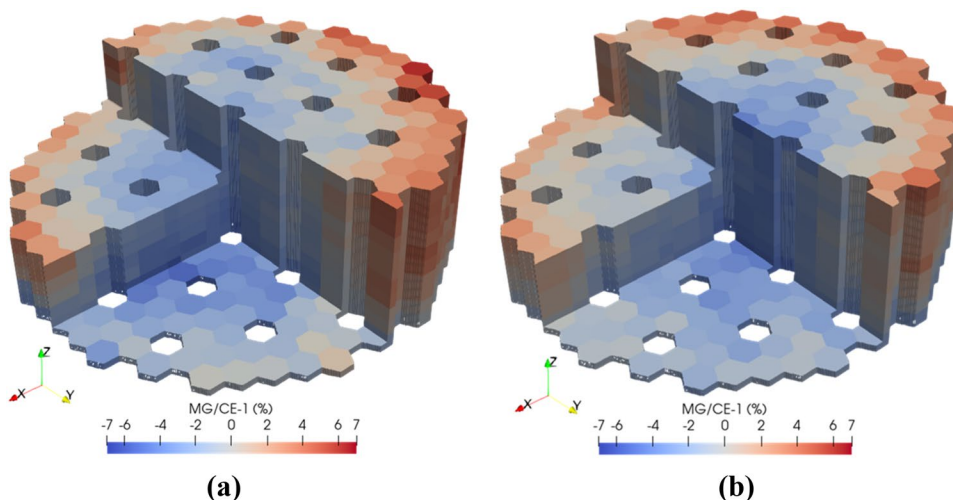
Remark: The statistical uncertainty of the OpenMC results is approximately ± 8 pcm. The results of the OECD/NEA Report are from Ref. [28]

**Table 5** Doppler constant in MET-1000 OECD/NEA benchmark (unit: pcm)

	BOC		EOC		EOC-BOC	
	$K_D$	MG-CE	$K_D$	MG-CE	$K_D$	MG-CE
OECD/NEA Report	347 ± 44	–	348 ± 36	–	–	–
CE	–358	–	–334	–	24	–
1-angle & Homo	–350	8	–350	–16	0	–23
32-angle & Homo	–365	–7	–338	–4	26	3
1-angle & LHete	–361	–3	–357	–23	3	–20
32-angle & LHete	–365	–7	–340	–6	25	1

Remark: The statistical uncertainty of the OpenMC results is approximately ± 8 pcm. The results of the OECD/NEA Report are from Ref. [28]

**Fig. 8** (Color online) 3D distribution of difference in power density between 32-angles & LHete and continuous-energy scheme at BOC ( $RRMSE=2.20\%$ ) (a) and EOC ( $RRMSE=2.06\%$ ) (b) in MET-1000 OECD/NEA benchmark



**3.1.5 Power distribution**

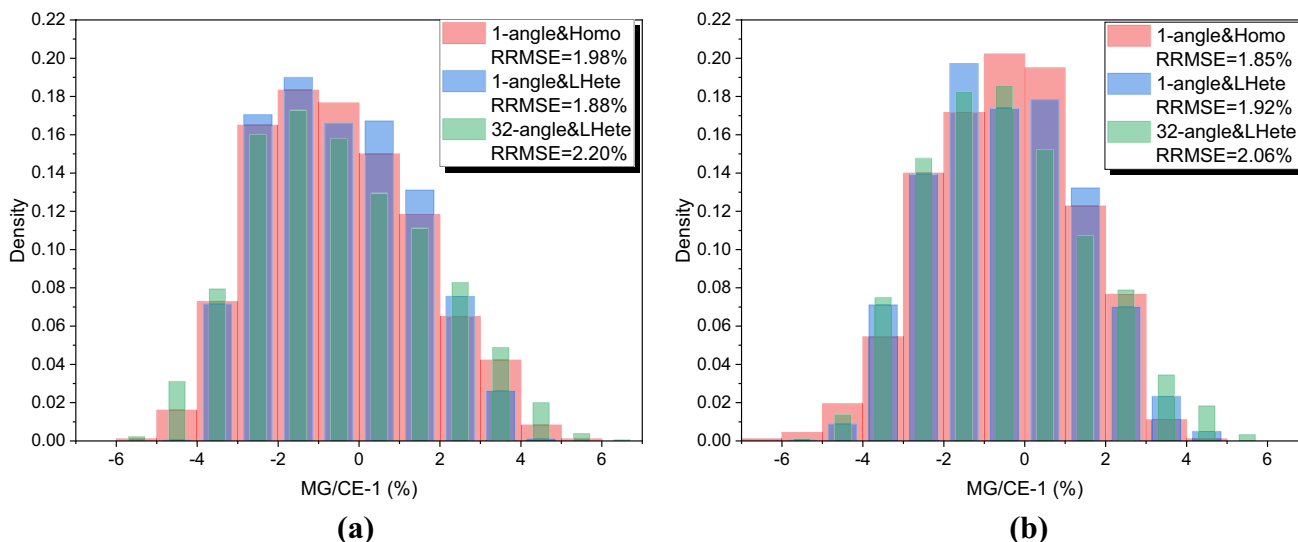
The 3D power distribution of the MET-1000 core, as determined by the CE schemes, is depicted in Fig. 7. Normalizing using the heating-local method reveals an average volume power density of  $272.6 \text{ W/cm}^3$  in the active zone. At the BOC, the peak and minimal power densities are  $397.0 \text{ W/cm}^3$  and  $133.4 \text{ W/cm}^3$ , respectively. By the EOC, these values change to  $385.6 \text{ W/cm}^3$  and  $133.0 \text{ W/cm}^3$ . The highest power density is observed in the outermost ring of the inner fuel zone.

Figure 8 illustrates the power distribution variance between the 32-angles & LHete and CE schemes. Radially, the 32-angles & LHete approach tends to overestimate power density in outer regions and underestimate it in the

inner regions. Axially, the upper zones show pronounced overestimation, whereas the lower zones indicate significant underestimation. The underlying reasons for this systematic disparity merit further investigation.

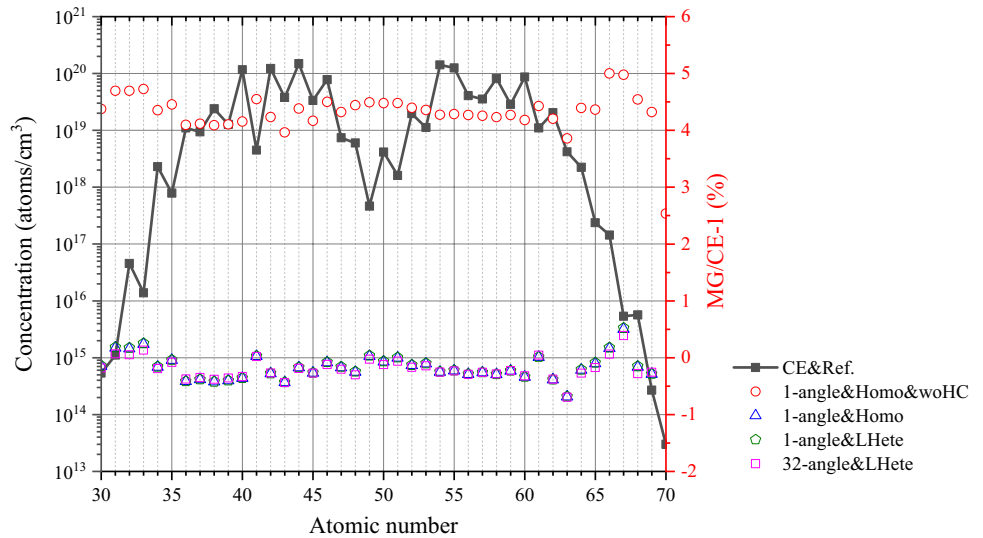
Figure 9 presents histograms of the relative difference between MG and CE schemes. The relative difference lies within a range of  $\pm 6\%$ . The average statistical standard deviation of this difference is approximately  $0.5\%$ . Both BOC and EOC show similar patterns. We used the relative root mean square error (RRMSE) to assess the performance of our models, calculated as follows:

$$RRMSE = \frac{\sqrt{\frac{\sum_{i=1}^N (p_{MG}^i - p_{CE}^i)^2}{N}}}{\bar{p}_{CE}} \tag{22}$$



**Fig. 9** (Color online) Histogram of difference between multi-group and continuous-energy schemes in power density at BOC (a) and EOC (b) in MET-1000 OECD/NEA benchmark

**Fig. 10** Concentration of fission products at EOC in MET-1000 OECD/NEA benchmark. Remark: woHC indicates the results without heating correction



where  $p_{MG}^i$  denotes the power density in region  $i$  as predicted by the MG solver,  $p_{CE}^i$  is the power density in region  $i$  according to the CE solver, and  $\bar{p}_{CE}$  represents the average power density. The computed RRMSE values for various approaches range between 1.85% and 2.06%.

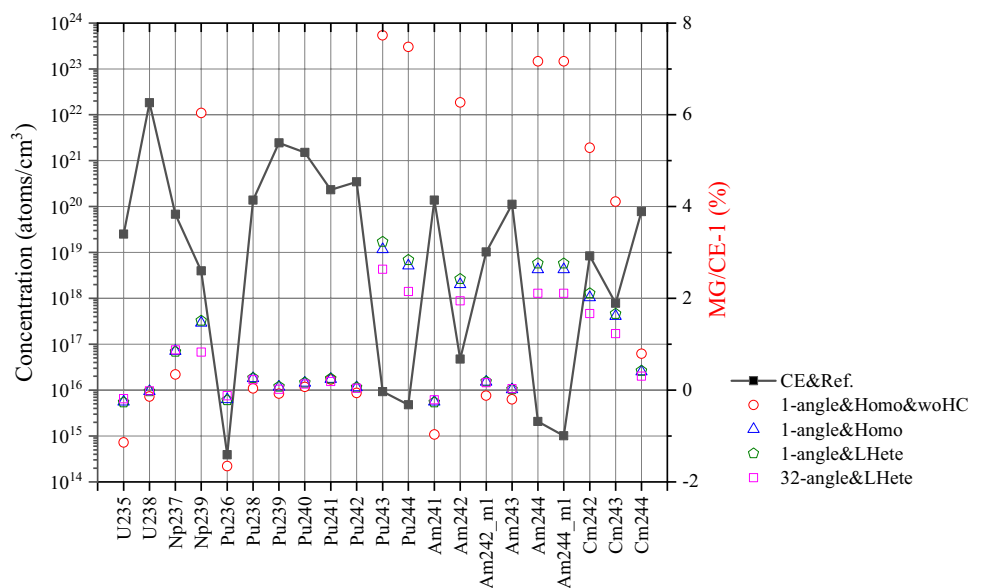
### 3.1.6 Concentration

Figure 10 presents the concentration of fission products (FPs) derived from the CE scheme. Over a single cycle, FPs accumulate to approximately  $1.23 \times 10^{21}$  atoms per  $\text{cm}^3$  in the metallic fuel. When excluding the heating-local correction, the MG scheme overpredicts FPs accumulation by approximately 4.2%, attributable to the overestimation of fuel burnup. Both the control rod geometry and relaxing

of FSA have minimal impact on FP accumulation. With the exception of europium (atomic number = 63), the discrepancy between the MG and CE schemes for individual elements remains within  $\pm 0.5\%$  when heating correction is applied. For the top 50 FP nuclides, this nuclide-specific variance is less than or equal to  $\pm 1.0\%$ .

Figure 11 illustrates the relative difference in concentrations of heavy nuclides. Without heating correction, this difference spans from  $-1.7\%$  to  $7.7\%$ . Applying heating correction significantly refines these differences, bringing them to a range of  $-0.3\%$  to  $3.1\%$  for the 1-angle scheme. Key nuclides such as  $^{235}\text{U}$ ,  $^{238}\text{U}$ ,  $^{237}\text{Np}$ ,  $^{238-242}\text{Pu}$ ,  $^{241}\text{Am}$ ,  $^{242\text{m}}\text{Am}$ , and  $^{243}\text{Am}$  exhibit discrepancies of less than 1%. However, there is a 2% to 3% overestimation for  $^{243}\text{Pu}$ ,  $^{244}\text{Pu}$ ,  $^{242}\text{Am}$ ,  $^{244}\text{Am}$ , and curium. The 32-angles scheme

**Fig. 11** Concentration of heavy nuclides at EOC in MET-1000 OECD/NEA benchmark. Remark: woHC indicates the results without heating correction



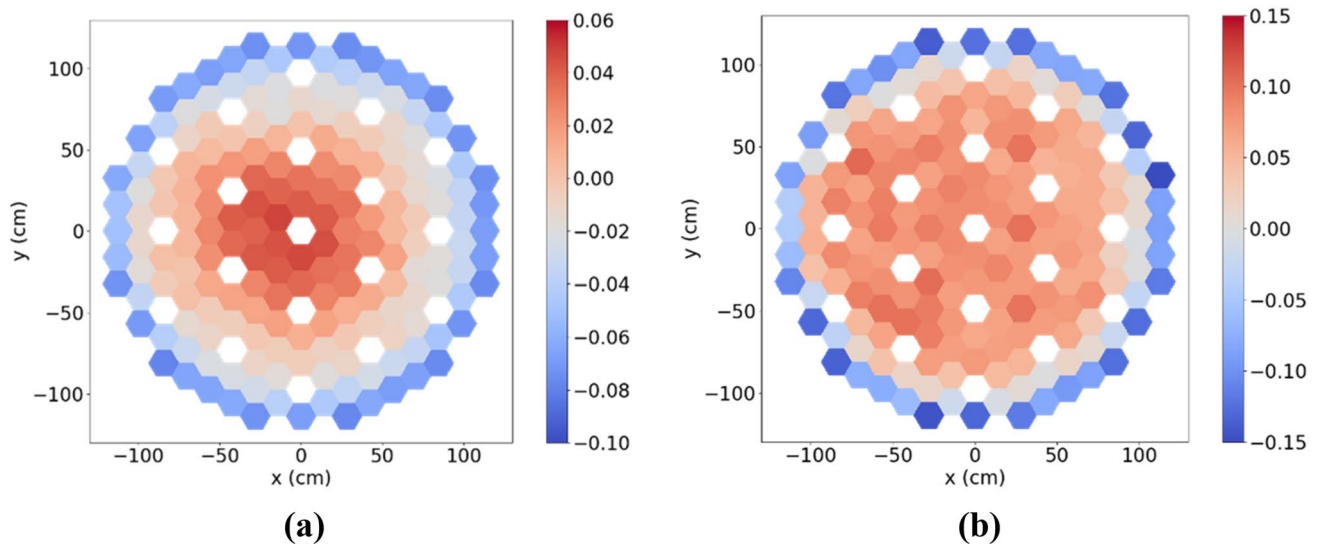


**Fig. 12** (Color online) Difference in concentration SA-by-SA of  $^{238}\text{U}$  (a) and  $^{239}\text{Pu}$  (b) at EOC in MET-1000 OECD/NEA benchmark (MG/CE-1 in unit %)

marginally corrects this overestimation, but the cause of the overestimation warrants further exploration.

Figure 12 depicts the differences in the SA-by-SA distribution of concentrations for  $^{238}\text{U}$  and  $^{239}\text{Pu}$ . The variation in  $^{238}\text{U}$  concentration lies between  $-0.1\%$  and  $0.06\%$ . For  $^{239}\text{Pu}$ , the range spans from  $-0.15\%$  to  $0.10\%$ . There is an overestimation of concentration in the inner regions and underestimation in the outer regions. This discrepancy corresponds to the power bias illustrated in Fig. 8. Due to reduced power in the inner region, there is less consumption of  $^{238}\text{U}$  and  $^{239}\text{Pu}$  throughout the cycle.

### 3.2 MET-1000 refueling benchmark

#### 3.2.1 Description of benchmark

Fuel management in fast reactors offers several choices. Batch loading involves replacing a portion of irradiated fuel

with new fuel at regular intervals. After several refuelings, the reactor can achieve an equilibrium fuel cycle with core characteristics similar to the previous cycle. While batch loading is crucial for fast reactor designs such as integral fast reactors, its accurate modeling is challenging due to the strong space and time dependencies. This scenario requires intricate 3D whole-core neutronics [30] calculations. The simulation of refueling is required for several cycles, and thus a mass of neutron transport and depletion calculations are required. Accurate prediction of reactivity, feedback coefficients, compositions, and power distribution in the refueling process is key to evaluating reactor performance. While the OECD/NEA benchmark divides the fuel into simple inner and outer zones with five axial subzones, refueling benchmarks scatter fuels with varying burnups. Thus, in addition to the one-cycle benchmark, this work introduces a multiple-cycle batch loading refueling benchmark.

**Table 6** Fresh fuel composition in MET-1000 refueling benchmark (unit: atoms/cm<sup>3</sup>)

Nuclide	Inner core	Outer core	Nuclide	Inner core	Outer core
$^{90}\text{Zr}$	$4.50947 \times 10^{22}$	$4.50965 \times 10^{21}$	$^{240}\text{Pu}$	$1.39086 \times 10^{22}$	$1.77766 \times 10^{21}$
$^{91}\text{Zr}$	$9.83407 \times 10^{21}$	$9.83446 \times 10^{20}$	$^{241}\text{Pu}$	$2.23706 \times 10^{21}$	$2.85919 \times 10^{20}$
$^{92}\text{Zr}$	$1.50316 \times 10^{22}$	$1.50322 \times 10^{21}$	$^{242}\text{Pu}$	$3.22320 \times 10^{21}$	$4.11958 \times 10^{20}$
$^{94}\text{Zr}$	$1.52332 \times 10^{22}$	$1.52338 \times 10^{21}$	$^{241}\text{Am}$	$1.47551 \times 10^{21}$	$1.88585 \times 10^{20}$
$^{96}\text{Zr}$	$2.45413 \times 10^{21}$	$2.45423 \times 10^{20}$	$^{242\text{m}}\text{Am}$	$9.47998 \times 10^{19}$	$1.21164 \times 10^{19}$
$^{235}\text{U}$	$5.14680 \times 10^{20}$	$4.87554 \times 10^{19}$	$^{243}\text{Am}$	$1.03850 \times 10^{21}$	$1.32731 \times 10^{20}$
$^{238}\text{U}$	$2.53582 \times 10^{23}$	$2.40216 \times 10^{22}$	$^{243}\text{Cm}$	$4.72045 \times 10^{10}$	$6.03321 \times 10^{09}$
$^{237}\text{Np}$	$7.74432 \times 10^{20}$	$9.89801 \times 10^{19}$	$^{244}\text{Cm}$	$6.11141 \times 10^{20}$	$7.81099 \times 10^{19}$
$^{238}\text{Pu}$	$1.30136 \times 10^{21}$	$1.66326 \times 10^{20}$	$^{245}\text{Cm}$	$1.40456 \times 10^{20}$	$1.79516 \times 10^{19}$
$^{239}\text{Pu}$	$2.28942 \times 10^{22}$	$2.92611 \times 10^{21}$	$^{246}\text{Cm}$	$9.32558 \times 10^{19}$	$1.19190 \times 10^{19}$

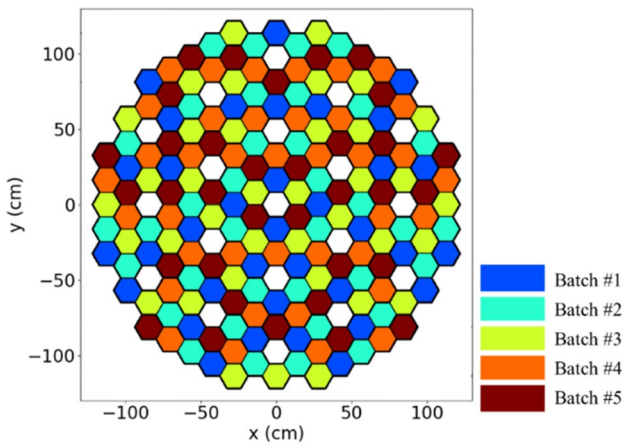
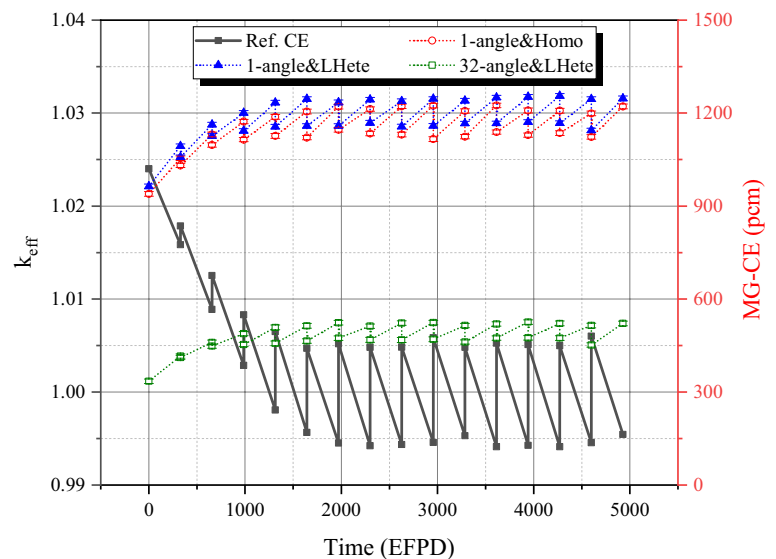


**Fig. 13** (Color online) Fuel batch map in MET-1000 refueling benchmark

This benchmark adopts the MET-1000 OECD/NEA core's geometry and structure. The initial cycle uses fresh fuel (composition in Table 6), with each cycle lasting 328.5 EFPD. About a fifth of the fuel is replaced with fresh fuel in each cycle, as depicted in Fig. 13. The refueling map of Fig. 13, designed for this work, ensures there is no local power peak from adjacent fuel SAs from the same batch. Due to computational demands, this benchmark uses the CASL chain with one step per cycle for depletion calculations. This choice has minimal impact on the discussed results, but its influence on other metrics, such as decay heat or radioactivity, requires further study. Expected results and definitions align with the OECD/NEA MET-1000 benchmarks.

In practical scenarios, it is imperative that the fuel composition and structural arrangement are meticulously designed. This ensures that the core maintains its criticality throughout

**Fig. 14** Trend of core reactivity in MET-1000 refueling benchmark



each cycle, requiring minimal excess reactivity. Between the shutdown for refueling and subsequent startup, there is a cooling period during which nuclides persistently decay. Transitioning a new core to its equilibrium cycle is intricate. The multi-cycle reloading study presented here serves as a representative model, emphasizing the pronounced spatial and temporal dependencies in neutronics modeling.

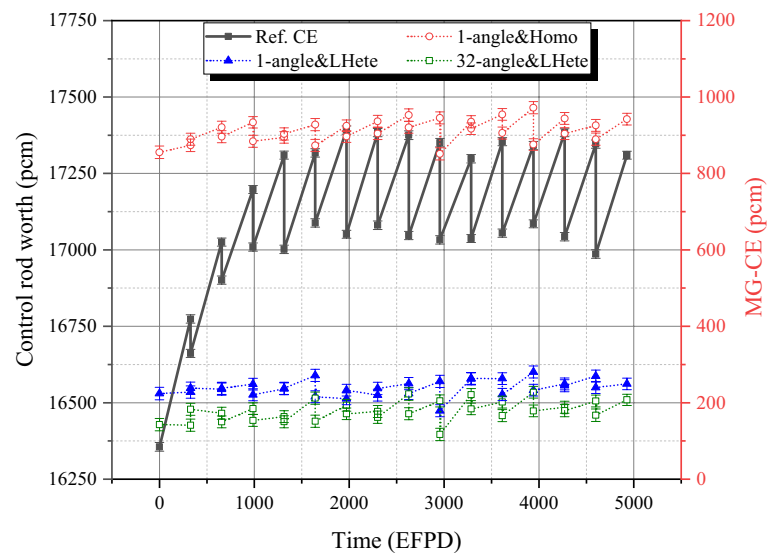
### 3.2.2 Reactivity

Figure 14 presents the variation of reactivity based on the CE calculation alongside the discrepancies between the MG and CE schemes. As fuel undergoes burnup, the core reactivity diminishes, experiencing surges with each refueling. After five cycles, each fuel SA within the core undergoes refueling at least once, leading to the establishment of an equilibrium state. As the transition to this state occurs, the overestimation of the MG schemes in core reactivity amplifies. This is attributed to accumulating differences in concentration (discussed in Sect. 3.2.6) and the compounded effects of the constant XS assumption. In an equilibrium cycle, the 1-angle MG scheme overestimates core reactivity by approximately 1204 pcm and the burnup reactivity loss by approximately 85 pcm; utilizing the 32-angle scheme reduces these overestimations to 494 pcm and approximately 59 pcm, respectively.

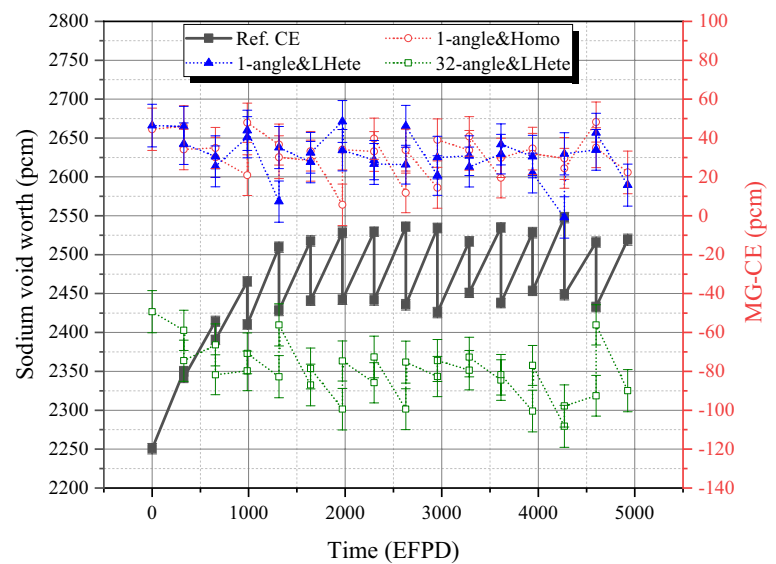
### 3.2.3 Control rod worth

Figure 15 illustrates the variation in control rod worth based on the CE scheme, as well as the differences between the MG and CE schemes. As we transition to the equilibrium cycle, the control rod worth escalates from 16,356 pcm to approximately 17,202 pcm. This increase is attributed to fluctuations

**Fig. 15** Trend of control rod worth in MET-1000 refueling benchmark



**Fig. 16** Trend of sodium void worth in MET-1000 refueling benchmark



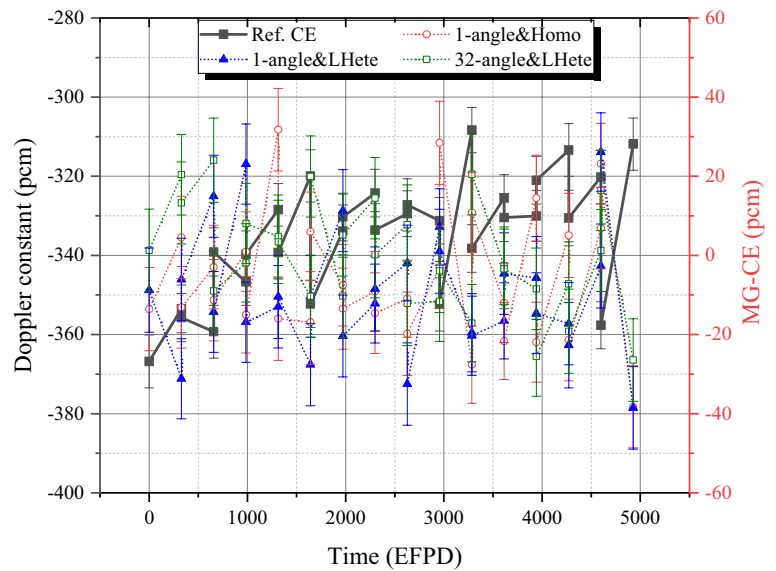
in burnup distribution and, consequently, flux distribution. The 1-angle&Homo scheme consistently overestimates reactivity, with values ranging between 851 and 972 pcm across 15 cycles. However, using the 1-angle&LHete scheme narrows this overestimation to between 179 and 280 pcm. Further refinement using the 32-angle&LHete scheme minimizes the overestimation even more, bringing it down to a range of 117 to 227 pcm.

### 3.2.4 Sodium void worth and Doppler constant

Figure 16 delineates the variation in sodium void worth based on the CE scheme and contrasts it with the differences observed between the MG and CE schemes. Starting

from 2,251 pcm in a pristine core state, the sodium void worth ascends to approximately 2,485 pcm upon reaching an equilibrium state. The 1-angle&Homo scheme tends to overestimate the sodium void worth, with deviations ranging from 6 to 48 pcm. Notably, the LHete has a minimal impact on predicting the sodium void worth, given that the control rods in this study are in an 'out-of-core' configuration. A more in-depth exploration is needed to understand the influence of control rod geometric heterogeneity on feedback coefficients during insertion depths. The 32-angle schemes, on the other hand, tend to underestimate the sodium void worth, with deviations ranging from  $-56$  to  $-108$  pcm. The discrepancy between the 32-angle and 1-angle schemes fluctuates between 98 and 148 pcm, a pattern that aligns closely with the findings

**Fig. 17** Trend of Doppler constant in MET-1000 refueling benchmark



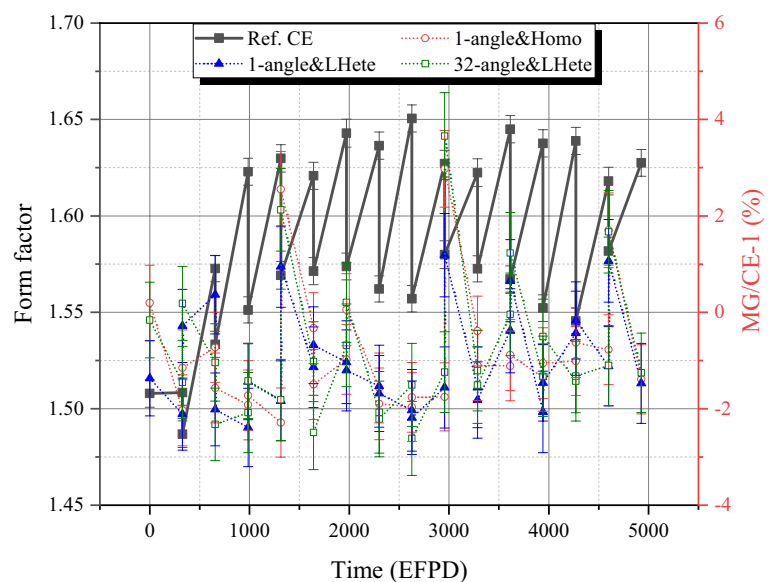
from the OECD/NEA MET-1000 benchmark (as discussed in Sect. 3.1.4).

Figure 17 contrasts the variation of the Doppler constant as determined by the CE calculation with the differences observed between the MG and CE schemes. The Doppler constant exhibits a statistical deviation of approximately 7 pcm, while the difference has a deviation of approximately 10 pcm. The Doppler constant ranges from  $-308$  to  $-367$  pcm, and the difference fluctuates between  $-38$  and  $31$  pcm. However, the statistical uncertainty is significant, rendering it challenging to make direct comparisons between the MG schemes.

### 3.2.5 Power distribution

Figure 18 illustrates the variation of the form factor in relation to refueling. Defined as the ratio of the maximum power density to the average power density, the form factor's resolution for maximum power is determined SA-by-SA radially and segmented into 10 axial subzones. From its initial value of 1.51 in a fresh core state, the form factor ascends to approximately 1.60 when the core reaches its equilibrium state. Notably, within each equilibrium cycle, the form factor experiences an increase from the BOC to the EOC. The discrepancy between the MG and CE schemes ranges from  $-2.5\%$  to  $4.0\%$ , with a RRMSE in power density distribution of approximately 2.2%.

**Fig. 18** Trend of form factor in MET-1000 refueling benchmark



**Fig. 19** (Color online) Power distribution at BOC of 15th cycle (a) and the relative difference between 32-angles&LHete and continuous-energy scheme (b) in MET-1000 refueling benchmark

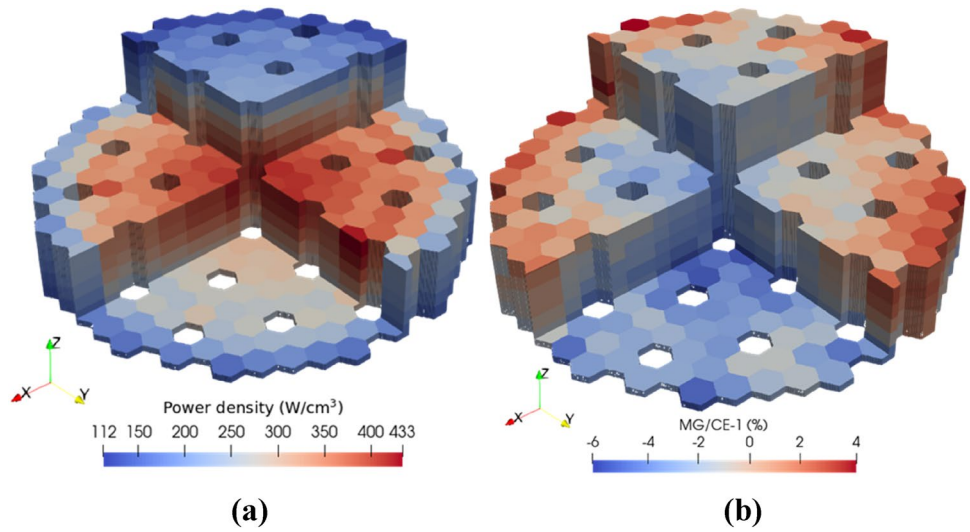


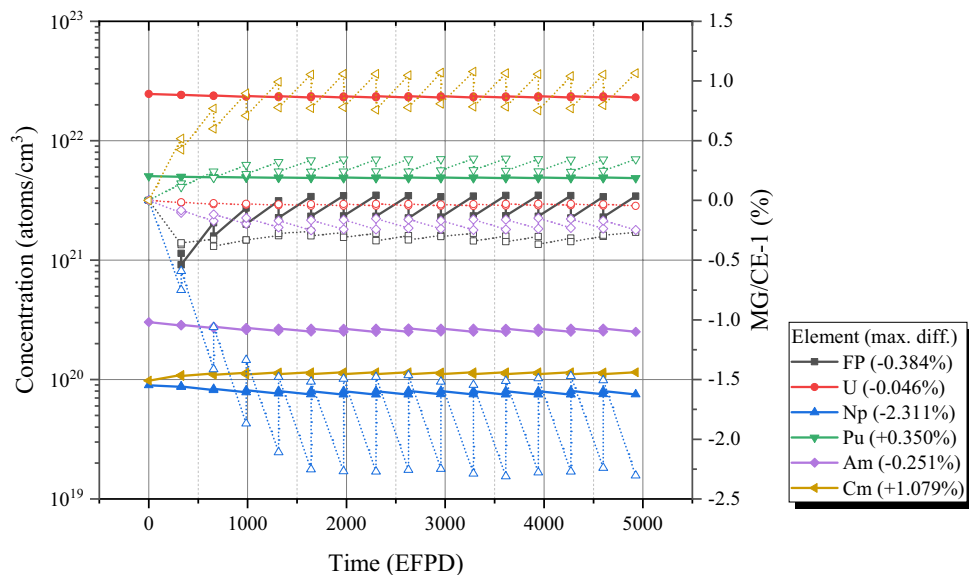
Figure 19 depicts the power distribution at the BOC for the 15<sup>th</sup> cycle. In the equilibrium state, fuels at various burnup levels are distributed sporadically. A notable high-power density can be observed at the core center and at the interface between the inner and outer core. The peak power is most pronounced in the fresh outer fuel (as illustrated in Batch #5 in Fig. 13) situated near the outermost control rods. The disparity between the MG and CE schemes mirrors the patterns observed in the OECD/NEA benchmark, as indicated in Fig. 8. However, this pronounced variation from the center to the periphery is disrupted by the uneven distribution of fuel burnup.

**3.2.6 Concentration**

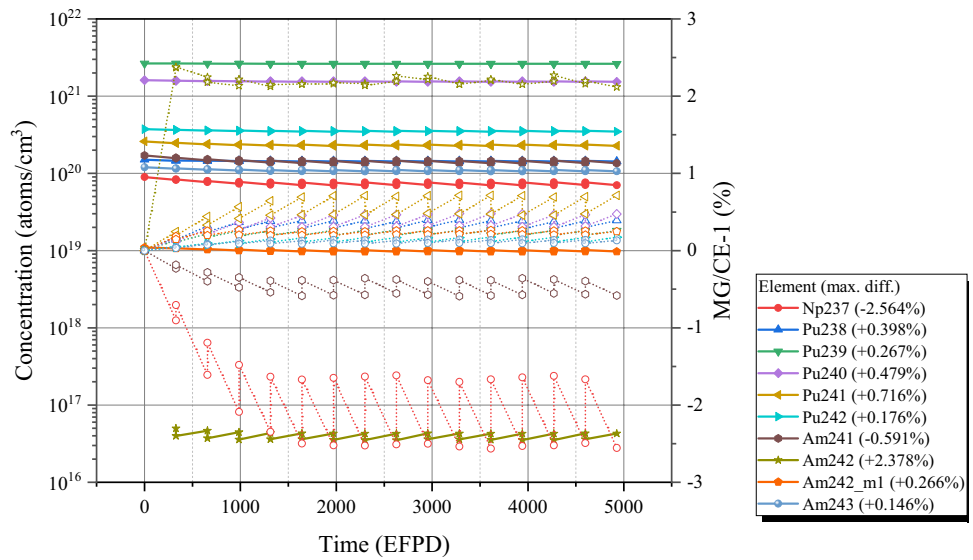
Figure 20 presents the variations in FPs and key actinide elements as they relate to refueling. As discussed in Sect. 3.1.6, the LHete and FSA have a negligible impact on concentration predictions. Hence, only the results corresponding to the 1-angle&LHete configuration are illustrated in Fig. 20. As the system transitions to the equilibrium cycle, discrepancies between the MG and CE accumulate with burnup. In equilibrium cycles, these discrepancies fluctuate, becoming more pronounced at the EOC compared to the BOC. The largest concentration differences for U, Pu, and Am remain below 0.5%. However, Np exhibits the most significant discrepancy, with a difference reaching -2.31%.

Table 6 highlights that the primary isotope of uranium is <sup>238</sup>U and with its variations and discrepancies further

**Fig. 20** Trend of fission products and key actinide elements in MET-1000 refueling benchmark. Remark: The solid line indicates concentration, while the dotted line indicates MG/CE-1



**Fig. 21** Trend of transuranium nuclides in MET-1000 refueling benchmark. Remark: The solid line indicates concentration, while the dotted line indicates MG/CE-1



**Table 7** Computational time for refueling benchmark (unit: CPU-hour)

Scheme	Chain	1-group XS Generation	33-group XS Generation	Core calculation	Total
CE	CASL				1143
CE	FULL				1742
1-angle MG	CASL	13	62	87	162
1-angle MG	FULL	31	62	108	201
32-angle MG	CASL	13	83	255	351

detailed in Fig. 20. Figure 21 provides a nuanced breakdown of the differences in transuranium nuclide concentrations. The MG scheme tends to underestimate the concentration of <sup>237</sup>Np by approximately -2.6% throughout the equilibrium cycle. Except for <sup>241</sup>Pu, the discrepancies for the main plutonium nuclides stay below 0.5%. The <sup>242</sup>Am discrepancy, at approximately 2.4%, emerges after the 1st cycle of irradiation and remains relatively stable thereafter. Given its short half-life and considerable absorption cross-section, <sup>242</sup>Am reaches a saturation concentration under irradiation. The continuous irradiation refueling scheme adopted in this study results in a stable discrepancy in the <sup>242</sup>Am concentration. Apart from <sup>242</sup>Am, concentration discrepancies for other americium isotopes stay under 0.6%.

### 3.2.7 Computational time

Table 7 lists the computation time required for a single refueling simulation in its standard state. The process involves 30 transport calculations and 15 depletion

calculations. Each transport calculation is configured with 100 inactive batches, 400 active batches, and 50,000 particles per batch. The time consumption between the homogenous and locally heterogeneous models is almost identical. Using the CASL chain, the computation time is reduced to 66% compared to the *full* chain. If the CASL chain is utilized, the 1-angle MG scheme reduces computation time by 86% when compared to the CE scheme. The angular-dependent MG scheme demands more computation time primarily due to core calculations.

The flux-moment homogenization techniques, as discussed in [31], can effectively calculate the impact of angle dependence while maintaining the 1-angle MGXS data format in the multi-group core calculation. Most of the computation time during core calculation is allocated to macroscopic cross-section preparation and particle transport simulation. Nonetheless, the macroscopic cross-section preparation module can be further optimized using parallel computing techniques.

It should be noted that the MG scheme will save more computation time if there are more core calculation cases, such as the optimization of fuel batch strategies, the insertion of control rods at different levels, the perturbation in certain nuclide concentrations, coupling with multiphysics analysis, and so on. In comparison to the Homo models predominantly utilized in the deterministic method, the LHte scheme would improve the depletion calculation of structures with complex or dramatic changes in flux level and spectrum, such as moderators [32], control rods, transmutation targets [33], and burnable poisons [34], which warrant further investigation.

## 4 Conclusion

This paper presents the development and verification of a MG depletion calculation scheme using OpenMC. The MGXS for core transport calculation derive from a 3D whole-core CE analysis. Depletion calculation cross-sections are synthesized from 3D core MGXS and 2D subassembly single-group cross-sections. Using this framework, we delved into locally heterogeneous core modeling and FSA. The MG scheme's validity was ascertained using a 1000 MWth metal-fueled fast reactor from the OECD/NEA benchmark and a refueling benchmark introduced in this paper. Metrics such as core reactivity, burnup reactivity swing, control rod worth, sodium void worth, Doppler constant, power distribution, and nuclide concentrations were compared against the CE depletion scheme.

In equilibrium cycles, the MG scheme, incorporating FSA, overestimates core reactivity by approximately 1150 pcm. Introducing a 32-angle relaxation diminishes this overestimation to approximately 450 pcm. The MG scheme with FSA presents a 150 pcm discrepancy in burnup reactivity swing due to biases in power distribution and microscopic cross-sections' burnup variation. The 32-angle relaxation reduces this discrepancy to 50 pcm.

For control rod worth, the MG scheme with homogeneous core modeling overestimates by approximately 5.3%. However, adopting a locally heterogeneous model reduces this to 1.4%. In the OECD/NEA benchmark, the FSA's impact on sodium void worth prediction is negligible, showing only a minor 20 pcm discrepancy. On the contrary, FSA overestimates sodium void reactivity by approximately 120 pcm compared to the relaxed spectrum adjustment. Differences in the Doppler constant remain minimal, oscillating between -40 and +30 pcm over 15 cycles in the refueling benchmark.

The relative disparity in power distribution stays within a  $\pm 6\%$  range. Differences between the MG and CE schemes in peak power density range from -2.5% to 4.0% during the refueling benchmark's 15 cycles. Concentration discrepancies remain within  $\pm 0.5\%$  for most elements in the OECD/NEA benchmark, with europium being a notable exception. For the top 50 FP nuclides, the disparity between MG and CE methods remains within  $\pm 1.0\%$ , a precision that persists in the refueling benchmark.

Broadly, the MG scheme employed in this research performs commendably for the MET-1000 metal-fueled fast reactor. It showcases versatility in modeling locally heterogeneous structures, maintaining consistency with the CE scheme. The locally heterogeneous approach holds promise for accurately addressing areas with stark neutron flux and spectrum changes. Future endeavors will explore innovative homogenization techniques to enhance FSA accuracy. We

also preliminarily validate OpenMC's capability for MGXS generation from whole-core modeling. Its integration with deterministic core transport calculation codes warrants further scrutiny. While our verification focuses on a medium-sized metal-fueled fast reactor, the scheme's precision in other reactor types, given their distinct burnup characteristics [35–37], necessitates additional validation.

**Acknowledgements** The computations in this paper were run on the  $\pi$  2.0 cluster supported by the Center for High-Performance Computing at Shanghai Jiao Tong University.

**Author contributions** All authors contributed to the study conception and design. Material preparation, data collection and analysis were performed by Hui Guo, Yi-Wei Wu, Qu-Fei Song, Yu-Yang Shen, Han-Yang Gu. The first draft of the manuscript was written by Hui Guo and all authors commented on previous versions of the manuscript. All authors read and approved the final manuscript.

**Data availability** The data that support the findings of this study are openly available in Science Data Bank at <https://www.doi.org/10.57760/sciencedb.j00186.00229> and <https://cstr.cn/31253.11.sciencedb.j00186.00229>.

## Declarations

**Conflict of interest** The authors declare that they have no competing interests.

## References

1. P.K. Romano, C.J. Josey, A.E. Johnson et al., Depletion capabilities in the OpenMC Monte Carlo particle transport code. *Ann. Nucl. Energy* **152**, 107989 (2020). <https://doi.org/10.1016/j.anucene.2020.107989>
2. T. Goorley, M. James, T. Booth et al., Initial MCNP6 release overview. *Nucl. Technol.* **180**, 298–315 (2012). <https://doi.org/10.13182/NT11-135>
3. D.P. Griesheimer, D.F. Gill, B.R. Nease et al., MC21 v.6.0 – A Continuous-Energy Monte Carlo Particle Transport Code with Integrated Reactor Feedback Capabilities, in: *SNA MC 2013 - Jt. Int. Conf. Supercomput. Nucl. Appl. Monte Carlo, EDP Sciences*, 2014: p. 06008. <https://doi.org/10.1051/snamc/20140600>
4. J. Leppänen, M. Pusa, T. Viitanen et al., The Serpent Monte Carlo code: status, development and applications in 2013. *Ann. Nucl. Energy* **82**, 142–150 (2015). <https://doi.org/10.1016/j.anucene.2014.08.024>
5. L. Deng, G. Li, B.-Y. Zhang et al., A high fidelity general purpose 3-D Monte Carlo particle transport program JMCT3.0. *Nucl. Sci. Tech.* **33**, 108 (2022). <https://doi.org/10.1007/s41365-022-01092-0>
6. K. Wang, Z. Li, D. She et al., RMC – A Monte Carlo code for reactor core analysis. *Ann. Nucl. Energy* **82**, 121–129 (2015). <https://doi.org/10.1016/j.anucene.2014.08.048>
7. H.-F. Liu, P. Ge, S.-P. Yu et al., Data decomposition method for full-core Monte Carlo transport–burnup calculation. *Nucl. Sci. Tech.* **29**, 20 (2018). <https://doi.org/10.1007/s41365-018-0366-4>
8. Y. Nagaya, K. Okumura, T. Mori et al., MVP/GMVP II : General purpose Monte Carlo Codes for neutron and photon transport calculations based on continuous energy and multigroup methods.

2004. <https://jopss.jaea.go.jp/pdfdata/JAERI-1348.pdf> (accessed June 8, 2022)
9. C.M. Perfetti, Advanced Monte Carlo Methods for eigenvalue sensitivity coefficient calculations. Thesis, 2012. <http://deepblue.lib.umich.edu/handle/2027.42/93973> (accessed June 8, 2022)
  10. M. Zangian, A. Minuchehr, A. Zolfaghari, Development and validation of a new multigroup Monte Carlo Criticality Calculations (MC3) code. *Prog. Nucl. Energy* **81**, 53–59 (2015). <https://doi.org/10.1016/j.pnucene.2015.01.007>
  11. A.G. Nelson, S. Shaner, W. Boyd et al., Incorporation of a multigroup transport capability in the OpenMC Monte Carlo Particle transport code. *Trans. Am. Nucl. Soc.* **117**, 679–681 (2017)
  12. C. Demaziere, *Modelling of nuclear reactor multi-physics* (Academic Press Inc, S.I., 2019)
  13. J. Leppänen, M. Pusa, E. Fridman, Overview of methodology for spatial homogenization in the Serpent 2 Monte Carlo code. *Ann. Nucl. Energy* **96**, 126–136 (2016). <https://doi.org/10.1016/j.anucene.2016.06.007>
  14. H.J. Park, H. Shim, H. Joo et al., Qualification test of few group constants generated from an MC method by the two-step neutronics analysis system McCARD/MASTER, Undefined. (2011). <https://www.semanticscholar.org/paper/QUALIFICATION-TEST-OF-FEW-GROUP-CONSTANTS-GENERATED-Park-Shim/5a84271a20a77dd754c0f298777f5dec2ef71dc7> (accessed March 21, 2022)
  15. W. Boyd, A. Nelson, P.K. Romano et al., Multigroup cross-section generation with the OpenMC monte carlo particle transport code. *Nucl. Technol.* **205**, 928–944 (2019). <https://doi.org/10.1080/00295450.2019.1571828>
  16. E. Nikitin, E. Fridman, K. Mikityuk, Solution of the OECD/NEA neutronic SFR benchmark with Serpent-DYN3D and Serpent-PARCS code systems. *Ann. Nucl. Energy* **75**, 492–497 (2015). <https://doi.org/10.1016/j.anucene.2014.08.054>
  17. H. Guo, K. Feng, Y. Wu et al., Preliminary verification of multigroup cross-sections generation and locally heterogeneous transport calculation using OpenMC with CEFR start-up tests benchmark. *Prog. Nucl. Energy* **154**, 104484 (2022). <https://doi.org/10.1016/j.pnucene.2022.104484>
  18. T.D.C. Nguyen, H. Lee, D. Lee, Use of Monte Carlo code MCS for multigroup cross section generation for fast reactor analysis. *Nucl. Eng. Technol.* **53**, 2788–2802 (2021). <https://doi.org/10.1016/j.net.2021.03.005>
  19. T.Q. Tran, A. Cherezov, X. Du, D. Lee, Verification of a two-step code system MCS/RAST-F to fast reactor core analysis. *Nucl. Eng. Technol.* **54**, 1789–1803 (2021). <https://doi.org/10.1016/j.net.2021.10.038>
  20. P.K. Romano, N.E. Horelik, B.R. Herman et al., OpenMC: a state-of-the-art Monte Carlo code for research and development. *Ann. Nucl. Energy* **82**, 90–97 (2015). <https://doi.org/10.1016/j.anucene.2014.07.048>
  21. H. Guo, E. Garcia, B. Faure et al., Advanced method for neutronic simulation of control rods in sodium fast reactors: numerical and experimental validation. *Ann. Nucl. Energy* **129**, 90–100 (2019). <https://doi.org/10.1016/j.anucene.2019.01.042>
  22. A.G. Nelson, W. Boyd, P.K. Romano, The effect of the flux separability approximation on multigroup neutron transport. *J. Nucl. Eng.* **2**, 86–96 (2021). <https://doi.org/10.3390/jne2010009>
  23. A. Lüthi, R. Chawla, G. Rimpault, Improved gamma-heating calculational methods for fast reactors and their validation for plutonium-burning configurations. *Nucl. Sci. Eng.* **138**, 233–255 (2001). <https://doi.org/10.13182/NSE01-A2211>
  24. P. Deng, B.K. Jeon, H. Park et al., Coupled neutron and gamma heating calculation based on VARIANT transport solutions. *Nucl. Sci. Eng.* **193**, 1310–1338 (2019). <https://doi.org/10.1080/00295639.2019.1621617>
  25. M. Pusa, Rational approximations to the matrix exponential in burnup calculations. *Nucl. Sci. Eng.* **169**, 155–167 (2011). <https://doi.org/10.13182/NSE10-81>
  26. M. Pusa, Higher-order Chebyshev rational approximation method and application to burnup equations. *Nucl. Sci. Eng.* **182**, 297–318 (2016). <https://doi.org/10.13182/NSE15-26>
  27. H. Guo, X. Peng, Y. Wu et al., Neutronics modelling of control rod compensation operation in small modular fast reactor using OpenMC. *Nucl. Eng. Technol.* **54**, 803–810 (2021). <https://doi.org/10.1016/j.net.2021.09.017>
  28. OECD/NEA, *Benchmark for neutronic analysis of sodium-cooled fast reactor cores with various fuel types and core sizes*, OECD/NEA, 2016
  29. T. Ogata, Metal fuel. *Compr. Nucl. Mater.* (2012). <https://doi.org/10.1016/B978-0-08-056033-5.00049-5>
  30. K. Devan, A. Riyas, P. Mohanakrishnan, Approach to equilibrium fuelling scheme of 500MWe PFBR based on 3-D core burnup modeling. *Nucl. Eng. Des.* **241**, 1596–1605 (2011). <https://doi.org/10.1016/j.nucengdes.2011.02.026>
  31. Y. Wu, Q. Song, K. Feng et al., Multigroup cross-sections generated using Monte-Carlo method with flux-moment homogenization technique for fast reactor analysis. *Nucl. Eng. Technol.* **55**, 2474–2482 (2023). <https://doi.org/10.1016/j.net.2023.04.011>
  32. K. Ohgama, T. Hara, H. Ohta et al., A design study on a metal fuel fast reactor core for high efficiency minor actinide transmutation by loading silicon carbide composite material. *J. Nucl. Sci. Technol.* **59**, 735–747 (2022). <https://doi.org/10.1080/00223131.2021.2005702>
  33. V. Pascal, R. Selabi, J. Tommasi, PHENIX: Interpretation of ECRIX-H transmutation experiment with TRIPOLI4D, in: MC 2017, Jeju, Korea, 2017
  34. H. Guo, P. Sciora, T. Kooyman et al., Application of boron carbide as burnable poison in sodium fast reactors. *Nucl. Technol.* **205**, 1433–1446 (2019). <https://doi.org/10.1080/00295450.2019.1620054>
  35. Z. Zhang, Y. Dong, Q. Shi et al., 600-MWe high-temperature gas-cooled reactor nuclear power plant HTR-PM600. *Nucl. Sci. Tech.* **33**, 101 (2022). <https://doi.org/10.1007/s41365-022-01089-9>
  36. B.H. Yan, C. Wang, L.G. Li, The technology of micro heat pipe cooled reactor: a review. *Ann. Nucl. Energy* **135**, 106948 (2020). <https://doi.org/10.1016/j.anucene.2019.106948>
  37. G. Sun, M. Cheng, Development of a MCNP5 and ORIGEN2 based burnup code for molten salt reactor. *Nucl. Sci. Tech.* **27**, 65 (2016). <https://doi.org/10.1007/s41365-016-0070-1>

Springer Nature or its licensor (e.g. a society or other partner) holds exclusive rights to this article under a publishing agreement with the author(s) or other rightsholder(s); author self-archiving of the accepted manuscript version of this article is solely governed by the terms of such publishing agreement and applicable law.